Chiral magnetism of magnetic adatoms generated by Rashba electrons

2017 New J. Phys. 19 023010

(http://iopscience.iop.org/1367-2630/19/2/023010)

New Journal of Physics
The open access journal at the forefront of physics

Deutsche Physikalische Gesellschaft DPG
IOP Institute of Physics

Published in partnership with: Deutsche Physikalische Gesellschaft and the Institute of Physics

OPEN ACCESS

RECEIVED
19 October 2016

REVISED
29 November 2016

ACCEPTED FOR PUBLICATION
19 December 2016

PUBLISHED
2 February 2017

PAPER

Chiral magnetism of magnetic adatoms generated by Rashba electrons

Juba Bouaziz[1,3], Manuel dos Santos Dias[1], Abdelhamid Ziane[1,2], Mouloud Benakki[2], Stefan Blügel[1] and Samir Lounis[1]

[1] Peter Grünberg Institut and Institute for Advanced Simulation, Forschungszentrum Jülich and JARA, D-52425 Jülich, Germany
[2] Laboratoire de Physique et Chimie Quantique, Faculté des Sciences, Université Mouloud Mammeri, 15000 Tizi-Ouzou, Algeria
[3] Author to whom any correspondence should be addressed.

E-mail: j.bouaziz@fz-juelich.de **and** s.lounis@fz-juelich.de

Keywords: Dzyaloshinskii–Moriya, Rashba electron gas, magnetic adatoms

Abstract

We investigate long-range chiral magnetic interactions among adatoms mediated by surface states spin-splitted by spin–orbit coupling. Using the Rashba model, the tensor of exchange interactions is extracted wherein a thepseudo-dipolar interaction is found, in addition to the usual isotropic exchange interaction and the Dzyaloshinskii–Moriya interaction. We find that, despite the latter interaction, collinear magnetic states can still be stabilized by the pseudo-dipolar interaction. The interadatom distance controls the strength of these terms, which we exploit to design chiral magnetism in Fe nanostructures deposited on a Au(111) surface. We demonstrate that these magnetic interactions are related to superpositions of the out-of-plane and in-plane components of the skyrmionic magnetic waves induced by the adatoms in the surrounding electron gas. We show that, even if the interatomic distance is large, the size and shape of the nanostructures dramatically impacts on the strength of the magnetic interactions, thereby affecting the magnetic ground state. We also derive an appealing connection between the isotropic exchange interaction and the Dzyaloshinskii–Moriya interaction, which relates the latter to the first-order change of the former with respect to spin–orbit coupling. This implies that the chirality defined by the direction of the Dzyaloshinskii–Moriya vector is driven by the variation of the isotropic exchange interaction due to the spin–orbit interaction.

Q1

1. Introduction

A lack of inversion symmetry, paired with strong spin–orbit (SO) coupling, generate the Dzyaloshinskii–Moriya (DM) interaction [1, 2], a key ingredient for non-collinear magnetism, which is at the heart of chiral magnetism. The DM interaction defines the rotation sense of the magnetization, rotating clockwise or counterclockwise along a given axis of a magnetic material. This is the case of spin-spirals in two-dimensional [3–5] or one-dimensional systems [6, 7] down to zero-dimensional non-collinear metallic magnets [8–10]. This type of interaction is decisive in the formation of the recently discovered magnetic skyrmions (see, e.g. [11–14]), a particular class of chiral spin texture, the existence of which was predicted three decades ago [15, 16]. These structures are believed to be interesting candidates for future information technology [17–20] since lower currents are required for their manipulation, in comparison to conventional domain walls [21, 22].

The ever-increasing interest in understanding the properties of the DM interaction and the corresponding vector is, thus, not surprising. Although the symmetry aspects of these interactions were discussed in the seminal work of Moriya [2], the ingredients affecting the magnitude and the particular orientation of a DM vector have been very little explored but are certainly related to the details of the electronic structure. In the context of long-range interactions mediated by conduction electrons, the DM interaction was addressed by Smith [23], and Fert and Levy [24]. They found a strong analogy with Ruderman–Kittel–Kasuya–Yosida (RKKY) interactions [25–27]. Indeed, the long-range DM vector oscillates in magnitude and changes its orientation as function of

distance, which was recently confirmed experimentally using scanning tunneling microscopy (STM) and theoretically using *ab initio* simulations based on density functional theory [8]. We note that today, besides theory, state-of-the-art STM experiments can be used to learn about the magnitude, oscillatory behavior and decay of RKKY interactions, as demonstrated in [28–30].

Our goal is to address the DM interaction in an analytically tractable model and investigate its magnitude, sign and direction following a bottom-up approach, assembling nanostructures of different sizes and shapes, atom-by-atom. We are particularly interested in the long-range magnetic interactions that have been already investigated several times theoretically. For example, Imamura *et al* [31] considered pairs of localized spins interacting via the so-called two-dimensional Rashba gas of electrons [32, 33] while Zhu *et al* [34] replaced the Rashba gas with the surface of a topological insulator. We revisit the case of Rashba electrons and consider particularly the surface state of Au(111), where the Rashba spin splitting was observed experimentally [35].[4] We report on selected nanostructures: dimers, wires, trimers, and two hexagonal structures deposited on the Au(111), where the interactions are mediated solely by the surface state. For the dimer case, we extract the analytical form of the magnetic exchange interactions tensor using the approximation of Imamura *et al* [31], labeled in the following RKKY approximation, without renormalizing the electronic structure of the Rashba electrons because of the presence of the nanostructures. We found an inconsistency in the forms derived in [31]; a neglected integrable singularity observed at the minima of the energy dispersion curve, which we discuss in the present article. Interestingly, we demonstrate that the magnetic interactions are intimately linked with the magnetization induced by the adatoms forming the dimers. We know, for instance, that a single magnetic adatom generates non-collinear magnetic Friedel oscillations, which can be decomposed into a linear combination of skyrmion-like magnetic waves [36]. The in-plane components of the induced magnetization define the DM interaction, while the out-of-plane component is related to the usual RKKY interaction. In addition, we go beyond the RKKY approximation by taking into account the impact of the deposited adatoms, which renormalize the electronic properties and can dramatically modify the long-range magnetic interactions. The multiple scattering treatment provides the justification for neglecting the contribution of the integrable singularity. Moreover, we find an pseudo-dipolar term, or a two-ion anisotropy term generated by the presence of SO coupling, which plays a crucial role in the magnetism of the nanostructures. Although not carefully studied in the literature, these interactions can reach a large magnitude and counteract the effect of the DM interaction by favoring collinear magnetism. After obtaining all magnetic interactions of interest, we use an extended Heisenberg model to investigate the magnetic states of the selected nanostructures.

2. Description of the model

The investigation of the magnetic behavior of the nanostructures is based on an embedding technique, where magnetic impurities are embedded on a surface characterized by the Rashba spin-splitted surface states. Once the electronic structure is obtained, we extract the tensor of the magnetic exchange interactions as given in an extended Heisenberg model utilizing the mapping procedure described below.

2.1. Rashba model and embedding technique

The two-fold degenerate eigenstates of a two-dimensional electron gas confined in a surface or an interface, i.e. a structure-asymmetric environment, experiences spin splitting induced by the SO interaction. Within the model of Bychkov and Rashba [32, 33], this splitting effect is described by the so-called Rashba Hamiltonian

$$\mathbf{H}_{\mathrm{R}} = \frac{p_x^2 + p_y^2}{2m^*}\,\mathbb{1}_2 - \frac{\alpha_{\mathrm{so}}}{\hbar}(\boldsymbol{\sigma}_x p_y - \boldsymbol{\sigma}_y p_x), \tag{1}$$

where p_γ, $\gamma \in \{x, y\}$, is the component of the momentum operator $\vec{p}$ in a Cartesian coordinate system with x, y coordinates in the surface plane whose surface normal points along $\hat{e}_z$, m^* is the effective mass of the electron, $\boldsymbol{\sigma}_\gamma$ are the Pauli matrices, and $\mathbb{1}_2$ is the unit matrix in spin-space, with the z-axis of the global spin frame of reference parallel to $\hat{e}_z$. α_{so} is the Rashba parameter, a measure of the strength of the SO interaction and the parameter that controls the degree of Rashba spin splitting.

The energy dispersion of the Rashba electrons is characterized by the k-linear splitting of the free-electron parabolic band dispersion:

$$E_{1(2)} = \frac{\hbar^2}{2m^*}(k_{1(2)}^2 - k_{\mathrm{so}}^2), \tag{2}$$

[4] We note that in addition to the Au(111) surface, several systems carry Rashba spin-splitted states (see, e.g. [47–52]).

with $k_{1(2)} = \sqrt{k_{so}^2 + \frac{2m^*E}{\hbar^2}} + (-)k_{so}$ and $k_{so} = \frac{m^*\alpha}{\hbar^2}$. For the case of the surface state of the Au(111) surface, $\alpha = -0.4$ eV Å and $m^* = 0.26\ m_e$ [37]. We want to calculate the magnetic interactions between magnetic adatoms immersed in a Rashba electron gas. Therefore, we use an embedding technique, where we connect the Rashba Green function $\boldsymbol{G}^0$ to the Green function $\boldsymbol{G}$ of the system Rashba electron gas and magnetic adatoms via a Dyson equation. $\boldsymbol{G}^0$, connecting two points separated by $\vec{R}$, is given by:

$$\boldsymbol{G}^0(\vec{R},\, E + \mathrm{i}\epsilon) = \begin{pmatrix} G_D & -G_{ND}\, e^{-i\beta} \\ G_{ND}\, e^{i\beta} & G_D \end{pmatrix}, \tag{3}$$

where G_D and G_{ND}, as defined in appendix A, depend on the position $\vec{R}$ and energy E, while β is the angle between $\vec{R}$ and the x-axis. When magnetic adatoms are present, the Green function connecting the adatoms sites i and j can be obtained from the Dyson equation:

$$\boldsymbol{G}_{ij}(E) = \boldsymbol{G}^0_{ij}(E) + \sum_{km} \boldsymbol{G}^0_{ik}(E)\, \boldsymbol{T}_{km}(E)\, \boldsymbol{G}^0_{mj}(E), \tag{4}$$

where $\boldsymbol{G}^0_{ij}(E)$ is the Rashba Green function connecting sites i and j. The full scattering matrix $\boldsymbol{T}(E)$ is given by a Dyson equation:

$$\boldsymbol{T}^{-1}_{ij}(E) = \boldsymbol{t}^{-1}_i(E)\delta_{ij} - \boldsymbol{G}^0_{ij}(E), \tag{5}$$

where $\boldsymbol{t}_i(E)$ is the single-site scattering matrix connected to the potential of a single adatom $\boldsymbol{v}_i$ via:

$$\boldsymbol{t}_i(E) = \boldsymbol{v}_i + \boldsymbol{v}_i\, \boldsymbol{G}^0_{ii}(E)\boldsymbol{t}_i(E), \tag{6}$$

In practice, we proceed to the s-wave approximation [36, 38] since the wavelength of Au(111) surface states at the Fermi energy and below are much larger than the size of a single adatom. In this approach, one can work with a single phase shift, $\delta_j(E)$, describing the scattering of the surface state at a single impurity: $\mathbf{t}_j = \frac{i\hbar^2}{m^*}(e^{2i\delta_j(E)} - 1)$ at site j.

2.2. Extended Heisenberg model

In the extended Heisenberg Hamiltonian H_m given in [39], the elements of the magnetic exchange tensor, $\mathbf{J}_{ij}$, can be extracted by differentiating H according to $\vec{e}_i$ and $\vec{e}_j$:

$$H_m = \sum_{i,j} \vec{e}_i\, \mathbf{J}_{ij}\, \vec{e}_j, \quad J^{\alpha\beta}_{ij} = \frac{\partial^2 H_m}{\partial e^\alpha_i\, \partial e^\beta_j}, \tag{7}$$

with $\{\alpha,\ \beta\} = \{x,\ y,\ z\}$ and $\vec{e}_i$ being the unit vector of the magnetic moment at site i. The exchange tensor is decomposed into three contributions:

$$\mathbf{J}_{ij} = \frac{1}{3}(\mathrm{Tr}\, \mathbf{J}_{ij})\mathbb{1}_3 + \mathbf{J}^A_{ij} + \mathbf{J}^S_{ij}. \tag{8}$$

In the right-hand side of equation (8), the first term is the isotropic exchange, while $\mathbf{J}^A_{ij}$ is the anti-symmetric part:

$$\mathbf{J}^A_{ij} = \frac{\mathbf{J}_{ij} - \mathbf{J}^T_{ij}}{2}, \tag{9}$$

which is connected to the DM vector components via:

$$\mathbf{J}^A_{ij} = \begin{pmatrix} 0 & D^z_{ij} & -D^y_{ij} \\ -D^z_{ij} & 0 & D^x_{ij} \\ D^y_{ij} & -D^x_{ij} & 0 \end{pmatrix}. \tag{10}$$

The last term of equation (8), $\mathbf{J}^S_{ij}$, is the symmetric part that describes pseudo-dipolar interactions:

$$\mathbf{J}^S_{ij} = \frac{\mathbf{J}_{ij} + \mathbf{J}^T_{ij}}{2} - \frac{1}{3}\,\mathrm{Tr}\{\mathbf{J}_{ij}\}\,\mathbb{1}_3. \tag{11}$$

For the Rashba model, we will see that there is a more natural way of decomposing the tensor, which is given in equation (18).

To find the magnetic ground state, we employ the magnetic exchange interaction tensor. We start from different initial configurations, evaluate the torque on each magnetic impurity and use it to iterate to new spin directions. Once the torque is below a numerical threshold, we take the magnetic configuration to define a candidate ground state. Then we compare the energies of the candidates and keep the one with the lowest energy.

2.3. Mapping procedure

The strategy is to consider the Hamiltonian describing the electronic structure of the nanostructures and perform the same type of differentiation as in equation (7) in order to identify the tensor of magnetic exchange interactions. We use Lloyd's formula [40], which permits the evaluation of the energy variation due to an infinitesimal rotation of the magnetic moments, starting from a collinear configuration [39, 41, 42]. In general, the contribution to the single-particle energy (band energy) after embedding the nanostructure is given by:

$$E_{\rm sp} = \frac{1}{\pi}\,{\rm Im}\int_{E_{\rm R}}^{E_{\rm F}} {\rm d}E\ {\rm Tr}\ln \boldsymbol{T}(E)^{-1}, \tag{12}$$

where $E_{\rm F}$ is the Fermi energy, $E_{\rm R} = -\frac{\hbar^2 k_{\rm so}^2}{2m^*}$ is the bottom of the Rashba energy bands and Tr is the trace over impurity position- and spin-indices. The elements of the tensor of exchange interaction are then given by

$$J_{ij}^{\alpha\beta} = \frac{\partial^2}{\partial e_i^\alpha \partial e_j^\beta} E_{\rm sp} = -\frac{1}{\pi}\,{\rm Im}\int_{E_R}^{E_F} {\rm d}E\ {\rm Tr}\ \frac{\partial^2}{\partial e_i^\alpha \partial e_j^\beta}\ln \boldsymbol{T}(E). \tag{13}$$

Using equation (5), we evaluate the required second derivative and find for the elements of the tensor of exchange interactions:

$$J_{ij}^{\alpha\beta} = -\frac{1}{\pi}\,{\rm Im}\int_{E_{\rm R}}^{E_{\rm F}} {\rm d}E\ {\rm Tr}\ \mathbf{t}_i^\alpha\,\mathbf{G}_{ij}\mathbf{t}_j^\beta\,\mathbf{G}_{ji}, \tag{14}$$

the trace is taken over the spin-index, and $\mathbf{t}_i^\alpha$ is simply the derivative of $\mathbf{t}$ with respect to e_i^α. Since the $\mathbf{t}$-matrix can be written as:

$$\mathbf{t} = \frac{t_\uparrow + t_\downarrow}{2}\,\mathbb{1}_2 + \frac{t_\uparrow - t_\downarrow}{2}\vec{\boldsymbol{\sigma}}\cdot\vec{e}, \tag{15}$$

we find that $\mathbf{t}_i^\alpha = \frac{\partial \mathbf{t}}{\partial e_i^\alpha} = \Delta_i\,\boldsymbol{\sigma}^\alpha$, with $\Delta = \frac{t_\uparrow - t_\downarrow}{2}$. The final form of the tensor of magnetic exchange interactions is then finally given by:

$$J_{ij}^{\alpha\beta} = -\frac{1}{\pi}\,{\rm Im}\int_{E_{\rm R}}^{E_{\rm F}} {\rm d}E\ \Delta_i\,\Delta_j\ {\rm Tr}\ \boldsymbol{\sigma}^\alpha\,\mathbf{G}_{ij}\,\boldsymbol{\sigma}^\beta\,\mathbf{G}_{ji}. \tag{16}$$

We see that equation (16) depends on the magnetic structure of the impurity cluster. In practice, we consider three different ferromagnetic configurations, aligned along the *x*-, *y*- and *z*-axes, compute the respective exchange tensors and keep the transverse blocks (e.g. for the ferromagnetic configuration along *z* we keep the *xy* block); elements that occur repeatedly are averaged.

3. Magnetic properties of dimers

3.1. RKKY approximation

Before the numerical evaluation of the exchange tensor in nanostructures from equation (16), it would be interesting to have an approximate analytic form. This is achievable by considering in equation (16) the unrenormalized Green functions, $\boldsymbol{G}^0$, instead of $\boldsymbol{G}$. Here we recover the RKKY approximation, expected from second-order perturbation theory and used, for example, in [31]. In the particular case of a two-dimensional Rashba electron gas, the Rashba Green function can be expressed using Pauli matrices:

$$\boldsymbol{G}_{ij}^0 = G_{\rm D}\,\boldsymbol{\sigma}_0 - i\,G_{\rm ND}(\cos\beta\,\boldsymbol{\sigma}_y - \sin\beta\,\boldsymbol{\sigma}_x). \tag{17}$$

Surprisingly, we found anisotropies in the diagonal part of the exchange tensor that are generally neglected in the literature. The physical meaning of these anisotropies can be traced back to the extended Heisenberg model defined by the tensor of magnetic exchange interactions. In fact, by defining the *x*-axis as the line connecting the two sites *i* and *j*, we show in appendix B that the extended Heisenberg Hamiltonian describing the corresponding magnetic coupling can be written as:

$$H_{\rm m} = J\,\vec{e}_i\cdot\vec{e}_j + D(\vec{e}_i\times\vec{e}_j)_y + I\,e_i^y\,e_j^y, \tag{18}$$

where the exchange constants (J, D and I) are related to the Rashba Green function by:

$$J = -\frac{2}{\pi}\,{\rm Im}\int_{E_{\rm R}}^{E_{\rm F}} {\rm d}E\ \Delta_i\,\Delta_j(G_{\rm D}^2 - G_{\rm ND}^2), \tag{19}$$

$$D = \frac{4}{\pi}\,{\rm Im}\int_{E_{\rm R}}^{E_{\rm F}} {\rm d}E\ \Delta_i\,\Delta_j\,G_{\rm D}\,G_{\rm ND}, \tag{20}$$

$$I = -\frac{4}{\pi}\,\mathrm{Im}\int_{E_R}^{E_F} \mathrm{d}E\;\Delta_i\,\Delta_j\,G_{ND}^2. \tag{21}$$

J is the isotropic exchange interaction, defined in this particular case (dimer along the x-axis) as $J = J_{ij}^{xx} = J_{ij}^{zz}$, which, if positive, favors an antiferromagnetic coupling in our convention, otherwise it favors a ferromagnetic coupling. D is the y-component of the DM vector, which is by symmetry the only non-zero component (third rule of Moriya [2]). This favors chiral magnetic textures lying in the xz plane. I is the pseudo-dipolar term, a two-ion anisotropy term, coming from the symmetric part of the exchange tensor. It leads to an anisotropy in the diagonal part of the tensor of the exchange interaction, for instance $J_{ij}^{xx} = J_{ij}^{zz} \neq J_{ij}^{yy}$. Considering the impurities along the x-axis, I is given by $J_{ij}^{yy} - J_{ij}^{zz}$. This anisotropy is finite because of the two-dimensional nature of the Rashba electrons, so the x- and y-directions are non-equivalent to the z-direction. Here, I favors a collinear magnetic structure along the y-axis and counteracts the DM interaction. The analytical forms of the magnetic exchange interactions allow us to understand their origin in terms of the magnetic Friedel oscillations generated by single atoms [36]. These oscillations carry a complex magnetic texture that can be interpreted in terms of skyrmionic-like waves. Within the RKKY approximation and neglecting the energy dependence of Δ_i, the isotropic interaction, J, connecting two impurities at sites i and j, is proportional to the z-component of magnetization generated at site j by a single impurity at site i. In other words, the impurity at site j feels the effective magnetic field generated by the magnetization at that site but induced by the adatom at site i. D, however, is defined by the in-plane component of the induced magnetization. This is a central result of our work. Here, the corresponding magnetic field felt by the second impurity has an in-plane component and naturally leads to a non-collinear magnetic behavior, i.e. the natural impact of the DM vector. I does not have a simple interpretation, but it can be related to the anisotropy (difference) of the induced magnetization parallel to the impurity moment upon its rotation from out-of-plane to in-plane. In the following we proceed to the analytical evaluation of (J, D, and I) from the equations above. The details of the integration are given in appendix C.

Evaluation of J. In order to derive analytically the exchange interactions, we use an approximation for the **t**-matrices. We assume that they are energy independent (resonant scattering for the minority-spin channel, i.e. $\delta_\downarrow = \frac{\pi}{2}$, and no scattering for the majority-spin channel, i.e. $\delta_\uparrow = \pi$), which allows us to write $\Delta_i = -\frac{2\mathrm{i}\hbar^2}{m^*}$. This approximation, used in [36], is reasonable for an adatom like Fe deposited on a Au(111) surface. Then, we find the asymptotic behavior of G_D and G_{ND} for large distances R (see appendix C). The isotropic exchange constant can be expressed as:

$$\begin{aligned} J &= \frac{2}{\pi^2 R}\,\mathrm{Im}\int_{E_R}^{E_F} \mathrm{d}E\;\frac{\mathrm{i}}{(k_1+k_2)^2}(k_1\,\mathrm{e}^{2\mathrm{i}k_1R} + k_2\,\mathrm{e}^{2\mathrm{i}k_2R}) \\ &= \frac{\hbar^2}{m^*\pi^2 R}\left[\frac{1}{2R}\sin(2k_FR)\cos(2k_{so}R) - k_{so}\sin(2k_{so}R)\;\mathrm{SI}(2k_FR)\right], \end{aligned} \tag{22}$$

where $\mathrm{SI}(x)$ is the sine-integrated function of x. J is found to be the sum of two functions. The first one evolves as a function of $\frac{1}{R^2}$, as expected for regular two-dimensional systems, but the second function decays like $\frac{1}{R}$, which has been neglected in the work of [31]. The $\frac{1}{R}$ decay leads to a slower decay of J than what is known for a regular two-dimensional electron gas. The origin of this term is the Van Hove singularity at the bottom of the two bands; the density of states of the Rashba electron gas resembles that of a one-dimensional electron gas between E_R and $E = 0$, where the two bands cross. At very large distances, $\mathrm{SI}(x)$ converges to a constant $\left(\frac{\pi}{2}\right)$ and J behaves like $\frac{1}{R}\sin(2k_{so}R)$. Naturally, when k_{so} is set to zero we recover the classical form of the RKKY interaction without SO coupling for a free-electron gas in two-dimensions, i.e. J evolves like $\frac{1}{R^2}\sin(2k_FR)$.

Evaluation of D**.** We consider the same approximations used above to calculate the y-component of the DM vector (D) and find:

$$\begin{aligned} D &= -\frac{4}{\pi^2 R}\,\mathrm{Im}\int_{E_R}^{E_F} \mathrm{d}E\;\frac{1}{2(k_1+k_2)^2}\,[k_1\,\mathrm{e}^{2\mathrm{i}k_1R} - k_2\,\mathrm{e}^{2\mathrm{i}k_2R}\,], \\ &= -\frac{\hbar^2}{m^*\pi^2 R}\left[\frac{1}{2R}\sin(2k_FR)\sin(2k_{so}R) + k_{so}\cos(2k_{so}R)\mathrm{SI}(2k_FR)\right]. \end{aligned} \tag{23}$$

Similar to the isotropic exchange constant, D is a sum of two terms. The first term decays as $\frac{1}{R^2}$ while the second as $\frac{1}{R}$. A perturbative development of D in terms of k_{so} shows that D is first order in SO coupling. At very large distances D evolves as $\frac{1}{R}\cos(2k_{so}R)$.

Evaluation of I**.** In appendix C, we show that I is a sum of two integrals over the energy because of a branch cut in the Hankel functions. The first integral, denoted I_1, goes from E_R to zero and the second, I_2, goes from zero to E_F.

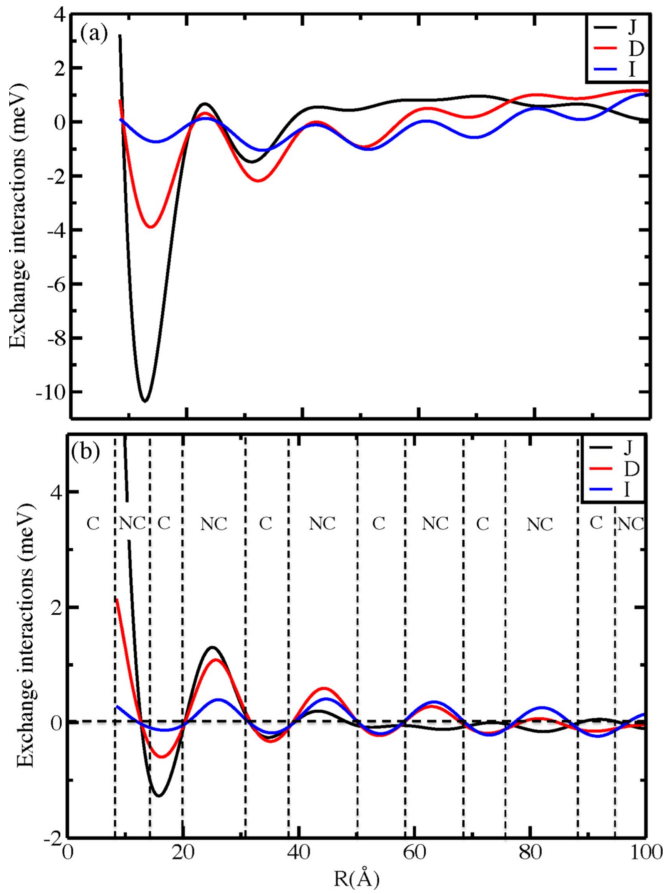

Figure 1. Evolution of the magnetic interactions J, D, and I (see equation (18)) as a function of distance, for $\alpha = -0.4$ eV Å and $m^* = 0.26\ m_e$ (parameters for the Au(111) surface [37] used in equation (1)). (a) We use the RKKY approximation (see equations (19), (20), and (21)) and assume a maximal scattering cross section for the minority-spin channel $\left(\delta_\downarrow = \frac{\pi}{2}\right)$ and no contribution for the majority-spin channel ($\delta_\uparrow = \pi$). (b) We go beyond the RKKY approximation and use the electronic structure renormalized by the presence of two impurities (equations (4) and (16)). The vertical lines define a magnetic phase diagram indicating the nature of the orientation of the two magnetic moments as function of their separation. C indicates the collinear phase of the magnetic moments and NC the non-collinear phase.

$$
\begin{aligned}
I_1 &= -\frac{4}{\pi^2 R}\,\mathrm{Im}\int_{E_R}^{0} \mathrm{d}E\ \frac{1}{2(k_1+k_2)^2} \\
&\quad\times [\mathrm{i}(k_1\,\mathrm{e}^{2\mathrm{i}k_1R} + k_2\,\mathrm{e}^{2\mathrm{i}k_2R}) + 2\sqrt{|k_1|k_2}\ \mathrm{e}^{\mathrm{i}(k_2-|k_1|)R}, \\
I_2 &= -\frac{4}{\pi^2 R}\,\mathrm{Im}\int_{0}^{E_F} \mathrm{d}E\ \frac{\mathrm{i}}{2(k_1+k_2)^2} \\
&\quad\times [\,k_1\,\mathrm{e}^{2\mathrm{i}k_1R} + k_2\,\mathrm{e}^{2\mathrm{i}k_2R} - 2\sqrt{k_1k_2}\ \mathrm{e}^{\mathrm{i}(k_1+k_2)R}\,],
\end{aligned}
\tag{24}
$$

and if we sum up the two terms:

$$
I = -J + \frac{\hbar^2}{m^*\pi^2 R}\left[\int_{|k_{so}|}^{k_F} \mathrm{d}q\ \sqrt{1-\frac{k_{so}^2}{q^2}}\ \cos(2qR) - \int_0^{|k_{so}|} \mathrm{d}q\ \sqrt{\frac{k_{so}^2}{q^2}-1}\ \sin(2qR)\right]. \tag{25}
$$

The integral involving $\cos(2qR)$ is important at short distances since it competes with one of the terms defining $-J$. In fact, it has the opposite sign of $-\frac{1}{2R}\sin(2k_FR)\cos(2k_{so}R)$ (see equation (22)). This reduces considerably the value of I compared to J. The second integral involves $\sin(2qR)$ and therefore it leads to a small contribution for low values of k_{so}. A perturbative development of I in terms of k_{so} shows that I is second order in SO coupling ($\propto k_{so}^2$).

In figure 1(a), we plot the magnetic exchange interactions J, D and I as function of the distance between two magnetic adatoms. The black curve depicts J, which at short distances is characterized by a wavelength $\lambda = \frac{\pi}{k_F} \approx 18.5$ Å. In figure 1(a) we see a beating of the oscillations, which can be understood by looking at the first term in equation (22). Writing it as $\frac{1}{4R}(\sin(2k_1R) + \sin(2k_2R))$, with $k_{1(2)} = k_F + (-)k_{so}$, the superposition of these two wave vectors causes a beating effect at $R_{so} = \frac{\pi}{4k_{so}} \approx 60$ Å. The finite value of J at R_{so} is

due to the second term in equation (22), since $\mathrm{SI}(2k_F R) \approx \frac{\pi}{2}$ and $\sin(2k_{so}R) \approx 1$. One notices that for a large range of distances ($R > 40$ Å) the magnetic interactions do not oscillate around the $y = 0$ axis, which is due to the $\mathrm{SI}(x)$ term present in equations (22) and (23) for J and D, while for I, the shift comes from the last term in equation (25). All these terms come from the Van Hove singularity at the bottom of the bands. Similar to J, D is negative for distances larger than 25 Å, which means that within the RKKY approximation the chirality defined by the sign of the DM interaction changes only for dimers separated by rather small distances. We notice also that D and I are oscillating functions that can be of the same magnitude as J. Thus, we believe that such systems provide the perfect playground to investigate large regions of the magnetic phase diagram inaccessible with the usual magnetic materials.

3.2. Beyond the RKKY approximation

The deposited magnetic impurities naturally renormalize the electronic properties of the Rashba electrons. We can now prove that the contributions of the sine integral to the magnetic interactions are artifacts of the RKKY approximation. When the energy approaches the Van Hove singularity, $E \rightarrow E_R = -\frac{\hbar^2 k_{so}^2}{2m^*}$, the multiple scattering series cannot be truncated, and the RKKY approximation cannot be made. The Green function connecting two impurities is given by:

$$\boldsymbol{G}_{12} = (1 - \boldsymbol{G}^0_{12}\, \boldsymbol{t}_2\, \boldsymbol{G}^0_{21}\, \boldsymbol{t}_1)^{-1}\, \boldsymbol{G}^0_{12} = \boldsymbol{G}^0_{12} + \boldsymbol{G}^0_{12}\, \boldsymbol{t}_2\, \boldsymbol{G}^0_{21}\, \boldsymbol{t}_1\, \boldsymbol{G}^0_{12} + \ldots, \tag{26}$$

where the second equality corresponds to the multiple scattering, or Born series. When $E \rightarrow E_R$, the Rashba Green function $\boldsymbol{G}^0_{12}(E) \rightarrow \infty$. However, from the first equality in equation (26), we have $\boldsymbol{G}_{12}(E) \rightarrow 0$ for $E \rightarrow E_R$, therefore, the Van Hove singularity will not contribute to the exchange interactions computed from equation (16) and the contribution from $\mathrm{SI}(x)$ vanishes.

To quantify the impact of the renormalization on the electronic states mediating the magnetic exchange interaction, we numerically compute $\boldsymbol{G}$, by considering consistently the multiple scattering effects. This is done first via considering an energy dependence in the $\mathbf{t}$-matrix, assuming that they correspond to a Lorentzian in the electronic structure of the impurities, and thus the phase shift is given by $\delta_\sigma(E) = \frac{\pi}{2} + \mathrm{atan}\left(\frac{E - E_\sigma}{\Gamma}\right)$. The parameters are extracted from first-principles electronic structure calculations [43]: the resonance width $\Gamma = 0.3$ eV, $E_\downarrow = 0.54$ eV for the minority-spin channel, slightly higher than the Fermi level $E_F = 0.41$ eV, and $E_\uparrow = E_\downarrow - 2.8$ eV due to exchange splitting. Then we use equation (5) for computing $\boldsymbol{T}(E)$. Afterwards we solve the Dyson equation (equation (4)) giving $\boldsymbol{G}$. The evolution of the three exchange interactions after renormalizing the Green function is given in figure 1(b). As expected, we note the disappearance of the RKKY approximation artifact leading to the apparent offset of the oscillations beyond $R = 40$ Å (see figure 1(a)). The beating effect in J occurs at the same distance as in the RKKY approximation because it is an intrinsic property of the Rashba electron gas. At large distances the intensities of J and D decrease quickly, but I keeps oscillating up to a distance of ≈200 Å where it decreases quickly to zero.

3.3. Magnetic configurations of dimers

Having established the behavior of the tensor of magnetic exchange interactions as a function of distance, we investigate now the magnetic ground state of different nanostructures characterized by different geometries and different sizes. After obtaining the magnetic interactions using the mapping procedure described in section 2.3, we minimize the extended Heisenberg Hamiltonian with respect to the spherical angles, (θ_i, ϕ_i), defining the orientation of every magnetic moment $\vec{e}_i = (\cos\phi_i \sin\theta_i,\ \sin\phi_i \sin\theta_i,\ \cos\theta_i)$. In order to check the stability of the magnetic ground state, we often add to the extended Heisenberg Hamiltonian the term $K\sum_i (e_i^z)^2$, where K is a single-ion magnetic anisotropy energy favoring an out-of-plane orientation of the magnetic moment, as is the case for an Fe adatom on Au(111). We choose as a typical value $K = -6$ meV for all the investigated nanostructures [44].

For the particular case of the dimer, an analytical solution is achievable by noticing that two magnetic states are possible: collinear (C) and non-collinear (NC). This is counter-intuitive, since the presence of the DM interaction leads usually to a non-collinear ground state. The presence of the pseudo-dipolar term I makes the physics richer and stabilizes collinear magnetic states. Once more, because of the particular symmetry provided by the Rashba electron gas, within the non-collinear phase, the only finite component of the DM vector, D_y, enforces the two magnetic moments to lie in the xz plane perpendicular to the DM vector. Within the collinear phase, I enforces the moments to point along the y-axis.

Non-collinear phase. Here the magnetic moments lie in the xz plane and the pseudo-dipolar term does not contribute to the ground state energy. The ground state is then defined by the angle, $\theta_0 = \mathrm{atan}\frac{D}{J}$, between the two magnetic moments at sites i and j. The energy corresponding to this state is $-|J|\sqrt{1 + \frac{D^2}{J^2}}$. With the single-ion anisotropy, K, the ground state angle becomes $\theta_0 = \mathrm{atan}\left(\frac{D}{J+K}\right)$. As an example, we consider two adatoms

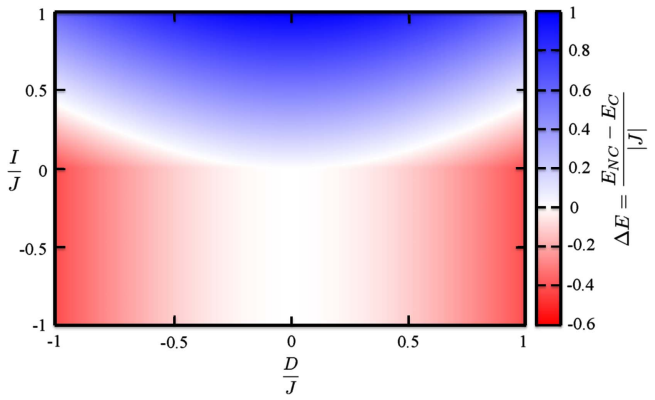

Figure 2. Phase diagram for the magnetic ground states of dimers. The color scale represents the energy difference normalized by $|J|$ between the non-collinear (red color) and collinear states (blue color) as function of the parameters $\left\{\frac{D}{J}, \frac{I}{J}\right\}$ (see equation (27)).

separated by $d = 10.42$ Å, which corresponds to the seventh nearest-neighbor distance on Au(111). In this case $J = 3.45$ meV and $D = 0.96$ meV and the ground state angle (θ_0) is 164° ($K = 0$ meV) or 171° ($K = -6$ meV).

Collinear phase. Here D does not contribute to the ground state configuration. When J and I are both negative the magnetic moments are parallel and point along the y-axis with energy $J + I$, while for positive J and I the magnetic moments are anti-parallel and also point along the y-axis, with energy $-(J + I)$. If J and I have opposite signs, for $J > 0$ the magnetic moments are anti-parallel in the (xz)-plane with energy $-J$, while for $J < 0$ the magnetic moments are parallel in the (xz)-plane with energy J. However, these last two solutions will not occur since the NC phase is lower in energy.

There is competition between the collinear phase C and the non-collinear phase NC, which depends on the involved magnetic interactions. Without I, figure 1(b) will consist of one single phase, the NC phase. Thanks to I, there is an alternation of the two phases depending on the interadatom distance. The magnetic anisotropy K favors an out-of-plane orientation of the moments and tends to decrease the spatial range of the collinear phase where the moments point along the y-axis.

Phase diagram. In figure 2, we plot the phase diagram of the dimers ($K = 0$ meV). The color scale shows the energy difference ΔE between the ground states found in the NC phase and C phase normalized by $|J|$. A negative (positive) energy difference corresponds to a NC (C) ground state. Thus the blue region corresponds to a C phase and the red region to a NC phase:

$$\begin{cases} \Delta E = \dfrac{E_{\mathrm{NC}} - E_{\mathrm{C}}}{|J|} = -\sqrt{1 + \dfrac{D^2}{J^2}} + 1 & \text{for } J \text{ and } I \text{ with opposite sign,} \\ \Delta E = \dfrac{E_{\mathrm{NC}} - E_{\mathrm{C}}}{|J|} = -\sqrt{1 + \dfrac{D^2}{J^2}} + \left(1 + \dfrac{I}{J}\right) & \text{for } J \text{ and } I \text{ with the same sign.} \end{cases} \tag{27}$$

For small ratios $\frac{D}{J}$, if $\frac{I}{J} < 0$ then $\frac{\Delta E}{|J|}$ simplifies to $-\frac{D^2}{2J^2}$ and if $\frac{I}{J} > 0$ it simplifies to $-\frac{D^2}{2J^2} + \frac{I}{J}$, which define the magnetic phases plotted in figure 2. We notice that when I and J are of the same sign, the dimers are mostly characterized by a C ground state. The corresponding C phase is separated from the NC phase by a parabola, as expected from the term $-\frac{D^2}{2J^2}$. Moreover we note that even within the NC phase, a transition occurs when the sign of $\frac{I}{J}$ changes. This is related to the nature of the NC phase that changes by switching the sign of $\frac{I}{J}$, which leads to an additional, $\frac{I}{J}$, term in the energy difference. As mentioned earlier, if $\frac{I}{J}$ is positive the moments are in-plane and align (parallel or anti-parallel) along the y-direction, while a negative $\frac{I}{J}$ leads to an alignment in the (xz) plane. For negative $\frac{I}{J}$, one notices that when $\frac{D}{J}$ goes to zero, the plotted energy difference goes to zero, which does not mean that the C and NC phases are degenerate, but it is the signature that the rotation angle of the moments goes to zero. Thus at $\frac{D}{J} = 0$ we have only a C phase.

Connecting J to D. Before investigating nanostructures containing more than two adatoms, it is interesting to analyze the possibility of connecting J to D. Recently, it was demonstrated that in the context of a micromagnetic model, the spin stiffness $A \sim \sum_j R_j^2 J(R_j)$, the micromagnetic counterpart of J, and $L = \sum_j R_j D(R_j)$, the counterpart of D called the Lifshitz invariant, can be related to each other for low SO interaction [45]:

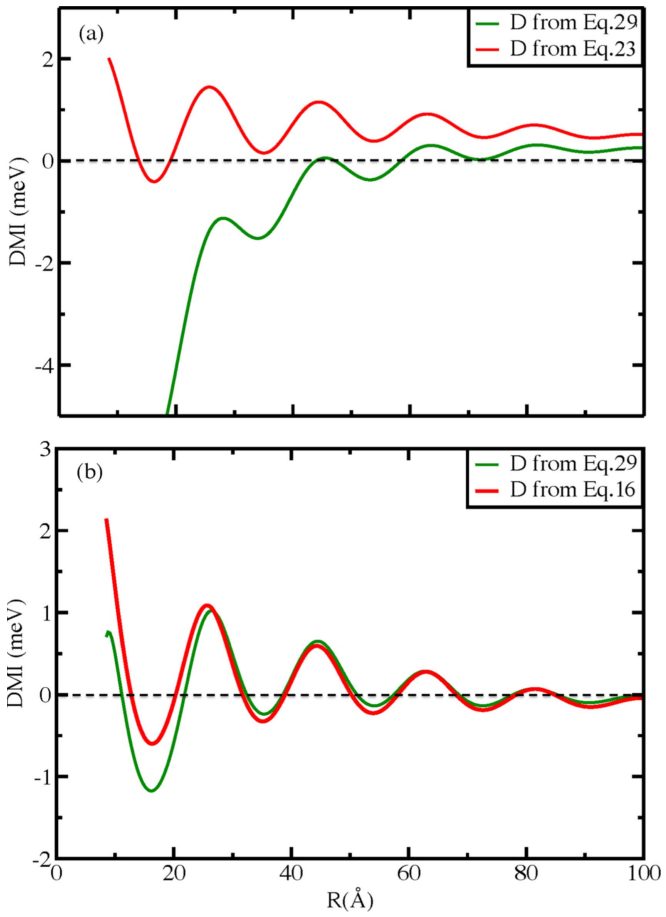

Figure 3. (a) Comparison between D computed from the RKKY approximation, equation (23), and from equation (29). (b) The comparison involves D computed from the renormalized Green functions equation (16), i.e. beyond the RKKY approximation, and from equation (29). As explained in the main text, the contribution from the Van Hove singularity that leads to the discrepancy seen in panel (a) is spurious.

$$L \sim -2k_{so}A. \tag{28}$$

The sum over sites j is limited by the size of the nanostructure but it can be infinite, e.g. if dealing with a monolayer or an infinite wire.

We checked the validity of the previous relation utilizing the analytical forms of J and D obtained in the RKKY approximation, i.e. equations (22) and (23), and found that equation (28) can be recovered for $k_{so}R \ll 1$ but the error is proportional to the term involving the sine integral $\mathrm{SI}(2k_F R)$. Therefore, if one neglects the contribution of the Van Hove singularity of the Rashba electron gas, one arrives at the formula of Kim *et al* [45]

However, we proved that the multiple scattering precisely cancels this extra contribution, so we propose the following relation to hold:

$$D = \frac{1}{2R}\frac{\partial J}{\partial k_{so}}. \tag{29}$$

First we compared the RKKY expressions in figure 3(a), inserting the result of equation (22) into equation (29), and then the RKKY expression for D given in equation (23). The agreement was very poor, as expected. Second, in figure 3(b) we extracted J from equation (16) and numerically evaluated equation (29), and then compared with D, also given by equation (16). So for the more realistic case (using the renormalized electronic structure) we found that equation (29) is a very good approximation. The intriguing implication of equation (29) is that it gives an interpretation for the origin of the chirality being left or right handed according to the sign of D. For a given distance R, D can be of the same (opposite) sign of J if the latter's magnitude increases (decreases) with the SO interaction.

4. Magnetic properties of other structures

In this section we build magnetic nanostructures of different sizes and shapes made of Fe adatoms deposited on Au(111) according to the parameters given in section 3.2. The distance between the first nearest neighbors is

Table 1. Summary of the average magnetic interactions between nearest neighbors for the calculated magnetic nanostructures. The values between parenthesis for the heptamer are for the nearest neighbors on the outer ring.

Structures	J (meV)	D (meV)	I (meV)	θ (°)
Chain	6.90	2.00	0.26	110
Trimer	3.51	1.00	0.13	117
Hexagon	5.64	1.67	0.23	164
Heptamer	4.69 (4.62)	1.37 (1.36)	0.18 (0.12)	120 (142)

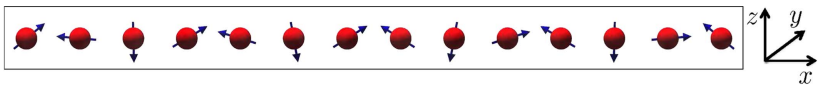

Figure 4. Magnetic ground state of a wire made of 14 adatoms. The interadatom distance is $d = 10.42$ Å, while the average nearest-neighbor isotropic exchange interaction is $J = 6.90$ meV and the nearest-neighbor DM vector points along the y-axis with an average intensity $D = 2$ meV. The magnetic anisotropy $K = 0$ meV. The spiral is characterized by an average rotation angle of 110° between nearest-neighbor magnetic moments.

chosen to be $d = 10.42$ Å for all structures, corresponding to the seventh nearest-neighbor distance on the Au(111) surface (lattice parameter $a = 2.87$ Å). This is very close to what is accessible experimentally [29].

We compute the magnetic interactions for the considered nanostructures. For the chosen interadatom distance for building the magnetic nanostructures, interactions beyond nearest neighbors play no significant role. For that reason, we report in table 1 only the average nearest-neighbor interactions, although all interactions are taken into account when determining the magnetic ground states. The z-component of the DM vector is two orders of magnitude smaller than the in-plane components for all the considered nanostructures, therefore it will be omitted when discussing the magnetic ground states. A summary of the obtained average magnetic interactions between nearest neighbors is provided in table 1.

4.1. Magnetism of linear chains

In addition to dimers, we investigated several linear chains of different sizes; all of them presented the same characteristics. Here we discuss the example of a wire made of 14 adatoms. In this case, the isotropic exchange interaction between the nearest neighbors is antiferromagnetic. On average it is equal to 6.90 meV, i.e. double the isotropic interaction obtained for the dimer, which highlights the impact of the nanostructure in renormalizing the electronic structure of the system. Within the RKKY approximation, the magnetic interactions would be independent of the nature, shape, size of the deposited nanostructures. Due to the Moriya rules, the DM vector lies along the y-direction within the surface plane, similar to the dimer case. It is thus perpendicular to the x-axis defined by the chain axis. The DM interaction is around 2 meV between nearest neighbors, i.e. once more double the value obtained for the dimer.

The magnetic ground state is a spiral contained in the (xz) plane with an average rotation angle of 110° between two nearest-neighbor magnetic moments (see figure 4). Interestingly, this angle is much smaller than the one found for the dimer (164°), but similar to that found for intermediate chain sizes. The pseudo-dipolar term is around $I = 0.26$ meV, and it has no impact on the ground state. This situation is equivalent to the NC phase of the dimer. Of course, choosing an interatomic distance with a large pseudo-dipolar term for the dimers leads generally to stable collinear magnetic wires (not shown here). We noticed that the effect of the magnetic anisotropy energy ($K = -6$ meV) is mainly on the edge atoms. Indeed, the rotation angles between adjacent inner moments remain at around 110°, while at the edges the magnetic moments point more along the z-direction. The rotation angle between the magnetic moment at the edge and the z-axis is reduced to 25°.

4.2. Magnetism of compact structures

After the one-dimensional case, we address in this section compact structures with the same interatomic distance as the one considered for the wire.

Trimer. We studied a trimer forming an equilateral triangle. The isotropic exchange constant J is equal to 3.51 meV, favoring antiferromagnetic coupling, a value close to the one found for the dimer. The frustration is large in this case, leading to a non-collinear ground state even without SO coupling [10, 46]. The magnetic moments lie in the same plane, e.g. the surface plane, with an angle of 120° between two magnetic moments. This state has continuous degeneracy, since rotating each magnetic moment in the same way leaves the energy

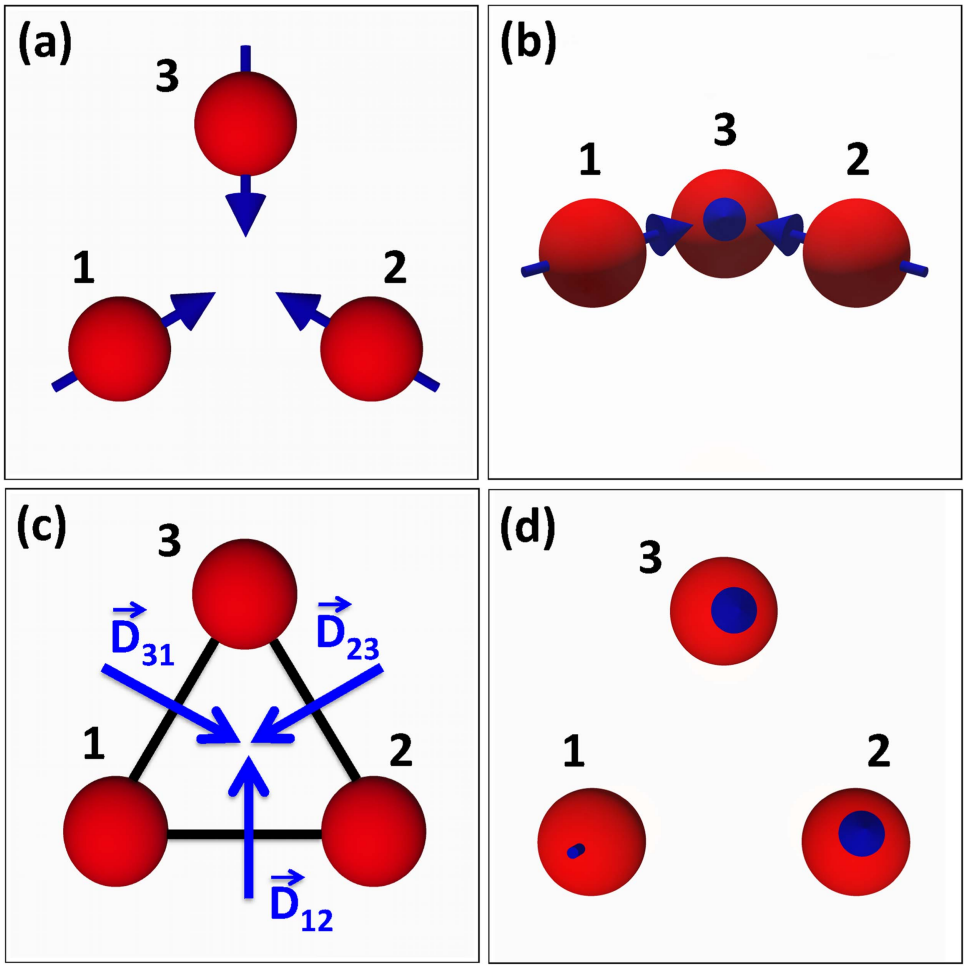

Figure 5. Non-collinear magnetic configuration for a trimer on an equilateral triangle shown from the top view (a) and side view (b). The interadatom distance $d = 10.42$ Å, while the isotropic exchange interaction is $J = 3.51$ meV and the intensity of the DM vector is $D = 1$ meV (for $K = 0$ meV). The antiferromagnetic J leads to the 120° configuration and the DM interaction induces a slight upward tilting of the magnetic moments. The corresponding DM vectors are plotted in (c). (d) Top view for the magnetic ground state of the trimer with $K = -6$ meV.

invariant. If we now consider the DM interaction, we find that $\vec{D}$, with a magnitude of 1.0 meV (similar to the dimer value), lies in the *xy*-plane and perpendicular to the axis connecting two adatoms (see figure 5(c)). This interaction lifts the degeneracy present without *D*, stabilizing the magnetic structure shown in figures 5(a) and (b). The pseudo-dipolar term *I* is equal to 0.13 meV and is small compared to *J* and *D*, therefore the non-collinear phase is more stable. The isotropic interaction keeps the angle between the in-plane projections of the moment at 120°, while the DM interaction generates a slight upward tilting (81° instead of 90°). In fact, every DM vector connecting two sites favors the non-collinearity of the related magnetic moments by keeping them in the plane perpendicular to the surface and containing the two sites. This is, however, impossible to satisfy at the same time for the three pairs of atoms forming the trimer, which leads to the compromise shown in figures 5(a) and (b). The magnetic anisotropy reduces ($K = -6$ meV) considerably the non-collinearity and the three moments are forced to point almost parallel to the *z*-axis. Two of the magnetic moments are characterized by an angle of 10° instead of 81° with respect to the *z*-axis, while the angle of the third moment is 173°, as shown in figure 5(d). This is an interesting outcome compared to the behavior of the wire, which is characterized by a large averaged DM interaction in comparison to the trimer. Obviously the shape of the nanostructure is important in stabilizing non-collinear magnetism. The interadatom distance is $d = 10.42$ Å, while the average nearest-neighbor isotropic exchange interaction is $J = 6.90$ meV and the nearest-neighbor DM vector points along the *y*-axis with an average intensity $D = 2$ meV. The magnetic magnetic anisotropy $K = 0$ meV.

Hexagon. We consider now a system of six atoms forming a hexagonal shape with the same interatomic distance as the one considered earlier. The magnetic ground state configuration is non-collinear as shown in figures 6(a) and (b). The isotropic magnetic exchange interaction, *J*, between nearest neighbors is of antiferromagnetic type, similar to the value obtained for the other nanostructures studied so far. *J* reaches a value of 5.64 meV, which is rather close to the interaction found for the wire. In fact one could consider this hexagonal

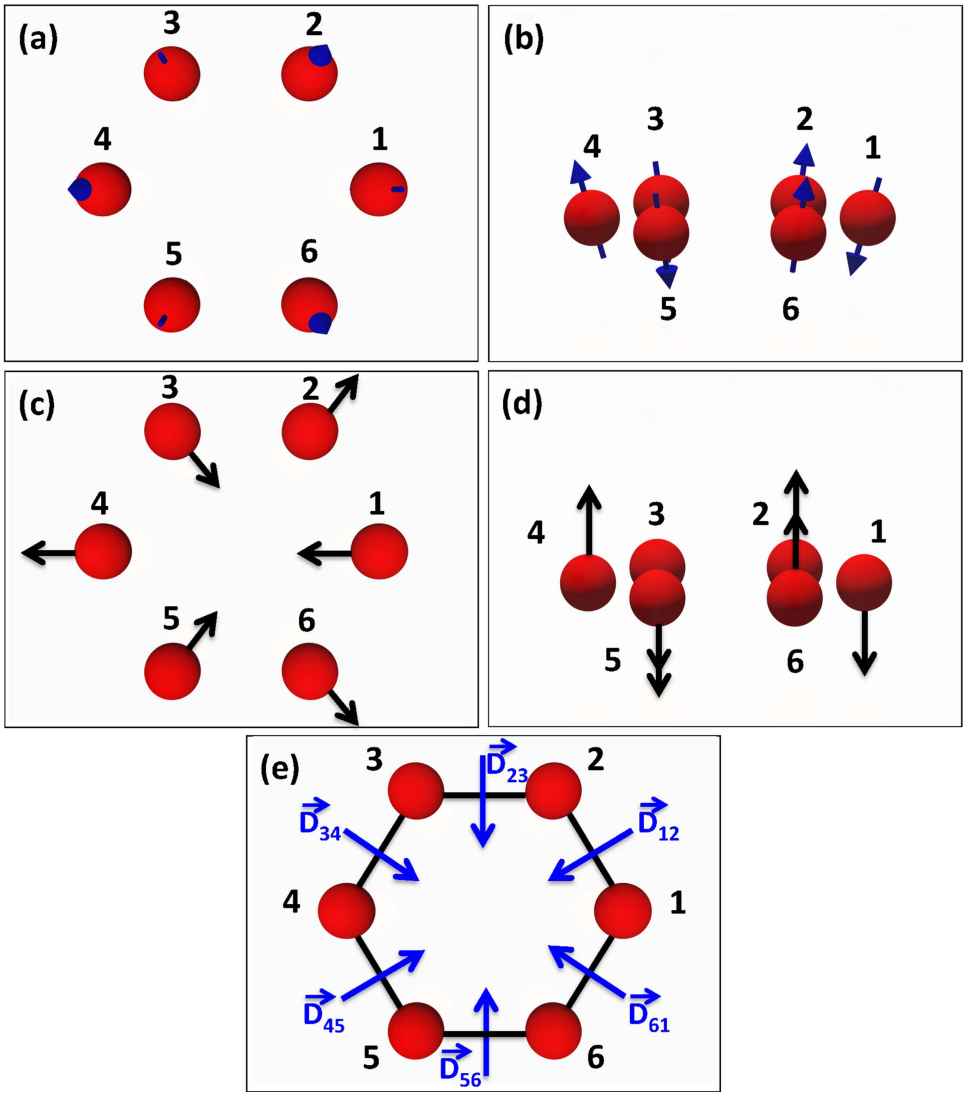

Figure 6. Top (a) and side (b) view of the magnetic ground state configuration for a hexagon made of six atoms. The interadatom distance is $d = 10.42$ Å, the nearest-neighbor isotropic exchange interaction is $J = 5.64$ meV and the intensity of the nearest-neighbor DM vector is $D = 1.67$ meV, while magnetic the anisotropy $K = 0$ meV. The projection of the unit vectors of the magnetic moments on the surface plane is given in (c) and the projection along the z-axis in (d). The corresponding DM vectors between the nearest neighbors are plotted in (e).

structure as a closed wire. The magnitude of the DM vector connecting two nearest neighbors is large, 1.67 meV, but not as large as the one of the wire. The non-collinear state is better appreciated when plotting the projection of the moment unit vectors on the surface plane in figure 6(c) and along the z-axis in figure 6(d). The polar angle is either 16° or 164°, according to the antiferromagnetic nature of the interactions. The azimuthal angle follows the symmetry of the hexagon, leading to an azimuthal angle difference of 120° between adjacent moments. The magnetic texture is a compromise involving the antiferromagnetic J and the DM vectors (plotted in figure 6(e)). While J tries to make the moments anti-parallel to each other, the DM vector tends to make them lie in the plane perpendicular to the surface and containing at the same time the two pairs of atoms (similar to the dimer configuration). However, the magnetic moment has to satisfy the DM vectors arising from its nearest neighbors and, therefore, the moment compromises and lies in the plane perpendicular to the surface, and containing the atom of interest and the center of the hexagon. This is similar to what was found for the compact trimer. To test the stability of the non-collinear structure, we add the magnetic anisotropy energy and the polar angles become either 9° or 171°), i.e. a change of ≈5°, which shows that K has a smaller impact on the hexagon than on the trimer.

Heptamer. We add to the previous structure an atom in the center of the hexagon. Contrary to the other atoms this central atom has six neighbors and the magnetic ground state is profoundly affected by this addition as shown in figures 7(a)–(b). The nearest-neighbor isotropic exchange constant J, 4.69 meV, decreases slightly in comparison to the value found for the open structure. The obtained magnetic texture can be explained from the

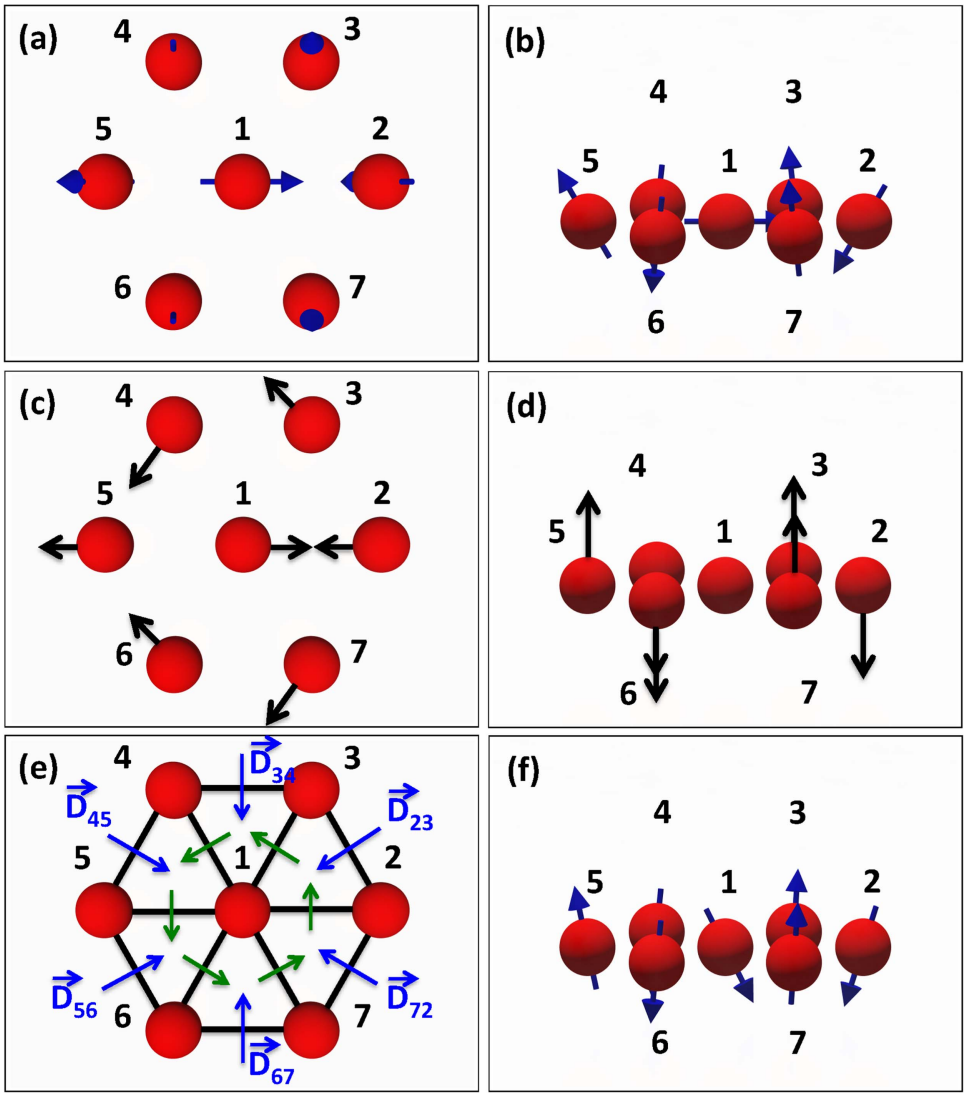

Figure 7. Non-collinear magnetic ground state found for the heptamer with an interadatom distance $d = 10.42$ Å, the nearest-neighbor isotropic exchange interaction is $J = 4.69(4.62)$ meV and the intensity of the nearest-neighbor DM vector is $D = 1.37(1.36)$ meV (the values between parenthesis are for the nearest neighbors on the outer ring), while the magnetic anisotropy $K = 0$ meV. (a) Top view and (b) Side view. The projection of the unit vectors of the magnetic moments on the surface plane is given in (c) and along the z-axis in (d). The corresponding DM vectors between the nearest neighbors are plotted in (e). (f) Side view of the ground state after adding a single-ion magnetic anisotropy, K, of -6 meV.

nearest-neighbor DM interaction (1.37 meV) with the corresponding vectors plotted in figure 7(e). The addition of the central atom creates frustration similar to the trimer case. Ideally, every pair of nearest-neighbor moments have to lie in the same plane. Thus, the central magnetic moment has to lie within one of the three planes orthogonal to the surface, and passing by two of the outer atoms and the central one. In this configuration, the three atoms are satisfied and the four atoms left have the direction of their moments adjusted, which leads to the final spin texture. Figures 7(c) and (d) show, respectively, the projection of the magnetic moment along the z-axis and in the surface plane. Interestingly, when the single-ion magnetic anisotropy is added only the central moment is affected. It experiences a switch from the in-plane configuration to a quasi out-of-plane orientation. A side view is shown in figure 7(f). This is another nice example showing how the stability of the non-collinear behavior is intimately related to the nature, shape, and size of the nanostructure.

5. Conclusions

We investigated the complex chiral magnetic behavior of nanostructures of different shapes and sizes wherein the atoms interact via long-range interactions mediated by Rashba electrons. We used an embedding technique based on the Rashba Hamiltonian and the s-wave approximation followed by a mapping procedure to an extended Heisenberg model. The analytical forms of the elements of the tensor of the magnetic exchange

interactions were presented within the RKKY approximation, i.e. without renormalizing the electronic structure due to the presence of the nanostructure. We demonstrated the deep link between the magnetic interaction and the components of the magnetic Friedel oscillations generated by the single adatoms. The isotropic interaction and the DM interactions corresponded, respectively, to the induced out-of-plane and in-plane magnetization. In addition to these two interactions, the pseudo-dipolar term, already found in [31], was shown to be large, generating a collinear phase competing with non-collinear structures induced by the DM interaction. We went beyond the RKKY approximation by considering energy dependent scattering matrices and multiple scattering effects to demonstrate that the size and shape of the nanostructures have a strong impact on the magnitude and sign of the magnetic interactions. We proposed an interesting connection between the DM interaction and the isotropic magnetic exchange interaction, J. The DM interaction can be related to the first-order change in J with respect to the SO interaction and, even more importantly, the origin of the sign of the DM interaction, i.e. defining the chirality, can be interpreted by the increase or decrease in J upon application of the SO interaction. We considered nano-objects that can be built experimentally (see e.g. [8, 29, 34]), and show that each of the objects behave differently and the stability of their non-collinear chiral spin texture is closely connected with the type of structure built on the substrate.

Acknowledgments

We gratefully acknowledge funding under HGF YIG Program VH-NG-717 (Functional Nanoscale Structure and Probe Simulation Laboratory–Funsilab), the ERC Consolidator grant DYNASORE and the DFG project LO 1659/5-1. SB acknowledges funding under the DFG-SPP 1666 'Topological Insulators: Materials—Fundamental Properties—Devices'. AZ thanks the Algerian Ministry of Higher Education and Scientific Research for funding his sabbatical year at the Forschungszentrum Jülich.

Appendix A

The Green function for the Rashba electron gas can be calculated using the spectral representation:

$$\boldsymbol{G}^0(\vec{r}, \vec{r}\,', E + \mathrm{i}\epsilon) = \sum_{\vec{k}n} \frac{\psi_{\vec{k}n}(\vec{r})\psi^*_{\vec{k}n}(\vec{r}\,')}{E - E_n + \mathrm{i}\epsilon}, \tag{30}$$

where E_n and $\psi_{\vec{k}}(\vec{r})$ are respectively the eigenvalues and eigenstates of the Rashba Hamiltonian. The Rashba Green function is translationally invariant, therefore $\boldsymbol{G}^0(\vec{r}, \vec{r}', E + \mathrm{i}\epsilon) = \boldsymbol{G}^0(\vec{R}, E + \mathrm{i}\epsilon)$, with $\vec{R} = \vec{r} - \vec{r}'$. After performing the sums over $\vec{k}$ and n, the diagonal and off diagonal spin elements of the Green function $\boldsymbol{G}^0$ of the Rashba electrons are given as:

$$G_{\mathrm{D}}(R, E + i\epsilon) = -\frac{im^*}{2\hbar^2(k_1 + k_2)}[k_1 H_0(k_1 R + i\epsilon) + k_2 H_0(k_2 R + i\epsilon)], \tag{31}$$

$$G_{\mathrm{ND}}(R, E + \mathrm{i}\epsilon) = -\frac{\mathrm{i}m^*}{2\hbar^2(k_1 + k_2)}[k_1 H_1(k_1 R + \mathrm{i}\epsilon) - k_2 H_1(k_2 R + \mathrm{i}\epsilon)]. \tag{32}$$

As mentioned in the main text, the vectors k_1 and k_2 are given by $k_1 = k_{\mathrm{so}} + \sqrt{k_{\mathrm{so}}^2 + \frac{2m^*E}{\hbar^2}}$ and $k_2 = -k_{\mathrm{so}} + \sqrt{k_{\mathrm{so}}^2 + \frac{2m^*E}{\hbar^2}}$ with $k_{\mathrm{so}} = \frac{m^*\alpha}{\hbar^2}$.

Appendix B

In this appendix we derive the generalized Heisenberg Hamiltonian $H_m = \vec{e}_i\, \mathbf{J}_{ij}\, \vec{e}_j$, which was simplified to the form given by equation (18). For this purpose, we need to calculate the elements of the tensor of exchange interactions showing up in equation (16), i.e. $\mathrm{Tr}\,\{\boldsymbol{\sigma}^\alpha\, \mathbf{G}_{ij}\, \boldsymbol{\sigma}^\beta\, \mathbf{G}_{ji}\}$, considering that $\mathbf{G}$ can be expressed in terms of G_{D} and G_{ND} (see equation (17)). This can be evaluated via the following trace (omitting the energy integration):

$$\begin{aligned} H_{\mathrm{m}} = \mathrm{Tr}\,[&(\vec{e}_{\mathrm{i}} \cdot \vec{\boldsymbol{\sigma}})(G_{\mathrm{D}}\, \boldsymbol{\sigma}_0 - \mathrm{i}\, G_{\mathrm{ND}}(\cos(\beta\boldsymbol{\sigma}_y) - \sin(\beta\boldsymbol{\sigma}_x)) \\ &\times (\vec{e}_j \cdot \vec{\boldsymbol{\sigma}})(G_{\mathrm{D}}\, \boldsymbol{\sigma}_0 + \mathrm{i}\, G_{\mathrm{ND}}(\cos(\beta\boldsymbol{\sigma}_y) - \sin(\beta\boldsymbol{\sigma}_x))]. \end{aligned} \tag{33}$$

Using the properties of the Pauli matrices, we know that for two vectors $\vec{A}$ and $\vec{B}$, the following relation holds: $(\vec{A} \cdot \vec{\boldsymbol{\sigma}})\,(\vec{B} \cdot \vec{\boldsymbol{\sigma}}) = (\vec{A} \cdot \vec{B})\,\boldsymbol{\sigma}_0 + i(\vec{A} \times \vec{B}) \cdot \vec{\boldsymbol{\sigma}}$. Thus:

$$\begin{aligned} H_{\rm m} &= 2\,\vec{e}_i\cdot\vec{e}_j(G_{\rm D}^2 - G_{\rm ND}^2) - 4(\vec{e}_i\times\vec{e}_j)_x\,{\rm i}\,G_{\rm D}\,G_{\rm ND}\sin\beta \\ &\quad - 4(\vec{e}_i\times\vec{e}_j)_y\,G_{\rm D}\,G_{\rm ND}\cos\beta + 4\,e_i^y\,e_j^y\,G_{\rm ND}^2\cos^2\beta \\ &\quad + 4\,e_i^x\,e_j^x\,G_{\rm ND}^2\sin^2\beta - 2(e_i^x\,e_j^y + e_i^y\,e_j^x)G_{\rm ND}^2\sin\beta\cos\beta. \end{aligned} \tag{34}$$

The terms proportional to $e_i^x\,e_j^x$ and $e_i^y\,e_j^y$ will lead to pseudo-dipolar-like terms after performing the energy integration given in equation (16). The terms proportional to $(e_i^x\,e_j^y + e_i^y\,e_j^x)$ are called interface terms. We can combine both terms in a pseudo-dipolar Hamiltonian for the two-dimensional case;

$$H_{\rm psd} = I\sum_{i,j}[(\vec{e}_i\cdot\vec{e}_j) - (\vec{e}_i\cdot\vec{R}_{ij})(\vec{e}_j\cdot\vec{R}_{ij}) - e_i^z\,e_j^z]. \tag{35}$$

$\vec{R}_{ij}$ is the vector connecting the impurities $\{i,j\}$.

If we consider that the two magnetic impurities are along the x-axis then $\beta = 0$ and we get the expression below for the trace:

$$H_{\rm m} = 2(G_{\rm D}^2 - G_{\rm ND}^2)\vec{e}_i\cdot\vec{e}_j - 4\,G_{\rm D}G_{\rm ND}\,(\vec{e}_i\times\vec{e}_j)_y + 4\,G_{\rm ND}^2 e_i^y\,e_j^y, \tag{36}$$

which leads to the final form of the Hamiltonian given in equation (18), and to the identification of the different magnetic interaction terms as presented in equations (22), (23), and (25).

Appendix C

In order to obtain the analytical forms of J, D and I in the RKKY approximation (equations (22), (23), and (25)), we evaluate the integrands needed in equations (19), (20), and (21) considering two regimes, positive or negative k_1. For $k_1 < 0$:

$$G_{\rm D}^2 = -\frac{(m^*)^2}{4\hbar^2(k_1+k_2)^2}[k_1^2H_0^{*2}(|k_1|R) + k_2^2H_0^2(k_2R) - 2\,k_1k_2H_0^*(|k_1|R)H_0(k_2R)], \tag{37}$$

$$G_{\rm ND}^2 = -\frac{(m^*)^2}{4\hbar^2(k_1+k_2)^2}[k_1^2H_1^{*2}(|k_1|R) + k_2^2H_1^2(k_2R) - 2\,k_1k_2H_1^*(|k_1|R)H_1(k_2R)], \tag{38}$$

and

$$\begin{aligned} G_{\rm D}G_{\rm ND} = -\frac{(m^*)^2}{4\hbar^2(k_1+k_2)^2}[&-k_1^2H_0^*(|k_1|R)H_1^*(|k_1|R) + k_1k_2\,H_0^*(|k_1|R)H_1(k_2R) \\ &+ k_1k_2\,H_1^*(|k_1|R)H_0(k_2R) - k_2^2H_1(k_2R)H_0(k_2R)]. \end{aligned} \tag{39}$$

For the case $k_1 > 0$:

$$G_{\rm D}^2 = -\frac{(m^*)^2}{4\hbar^2(k_1+k_2)^2}[k_1^2H_0^2(k_1R) + k_2^2H_0^2(k_2R) + 2k_1k_2H_0(k_1R)H_0(k_2R)], \tag{40}$$

$$G_{\rm ND}^2 = -\frac{(m^*)^2}{4\hbar^2(k_1+k_2)^2}[k_1^2H_1^2(k_1R) + k_2^2H_1^2(k_2R) - 2k_1k_2H_1(k_1R)H_1(k_2R)], \tag{41}$$

and

$$\begin{aligned} G_{\rm D}\,G_{\rm ND} = -\frac{(m^*)^2}{4\hbar^2(k_1+k_2)^2}[&k_1^2H_0(k_1R)H_1(k_1R) - k_1k_2H_0(k_1R)H_1(k_2R) \\ &+ k_1k_2H_1(k_1R)H_0(k_2R) - k_2^2H_0(k_2R)H_1(k_2R)]. \end{aligned} \tag{42}$$

We use the asymptotic expansion for the Hankel functions for large R: $H_0(x) \simeq \sqrt{\frac{2}{\pi x}}\,{\rm e}^{{\rm i}(x-\frac{\pi}{4})}$ and $H_1(x) \simeq \sqrt{\frac{2}{\pi x}}\,{\rm e}^{{\rm i}(x-\frac{3\pi}{4})}$ which simplify the previous forms for negative $k_1 < 0$ to:

$$G_{\rm D}^2 = \frac{{\rm i}(m^*)^2}{2\hbar^2(k_1+k_2)^2\pi R}\,[-|k_1|\,{\rm e}^{-2{\rm i}|k_1|R} + k_2\,{\rm e}^{2{\rm i}k_2R} + 2{\rm i}\,\sqrt{|k_1|k_2}\,\,{\rm e}^{(k_2-|k_1|)R}\,], \tag{43}$$

$$G_{\rm ND}^2 = -\frac{{\rm i}(m^*)^2}{2\hbar^2(k_1+k_2)^2\pi R}\,[-|k_1|\,{\rm e}^{-2{\rm i}|k_1|R} + k_2\,{\rm e}^{2{\rm i}k_2R} - 2{\rm i}\,\sqrt{|k_1|k_2}\,\,{\rm e}^{(k_2-|k_1|)R}\,], \tag{44}$$

and

$$G_{\rm D}\,G_{\rm ND} = \frac{(m^*)^2}{2\hbar^2(k_1+k_2)^2\pi R}\,[\,-|k_1|\,{\rm e}^{-2{\rm i}|k_1|R} - k_2\,{\rm e}^{2{\rm i}k_2R}\,]. \tag{45}$$

While a positive k_1 leads to:

$$G_{\mathrm{D}}^2 = \frac{\mathrm{i}(m^*)^2}{2\hbar^2(k_1+k_2)^2\pi R}\left[\, k_1\, \mathrm{e}^{2\mathrm{i}k_1R} + k_2\, \mathrm{e}^{2\mathrm{i}k_2R} + 2\sqrt{k_1k_2}\, \mathrm{e}^{\mathrm{i}(k_1+k_2)R}\,\right], \tag{46}$$

$$G_{\mathrm{ND}}^2 = -\frac{\mathrm{i}(m^*)^2}{2\hbar^2(k_1+k_2)^2\pi R}\left[\, k_1\mathrm{e}^{2\mathrm{i}k_1R} + k_2\, \mathrm{e}^{2\mathrm{i}k_2R} - 2\sqrt{k_1k_2}\, \mathrm{e}^{\mathrm{i}(k_1+k_2)R}\,\right], \tag{47}$$

and

$$G_{\mathrm{D}}\, G_{\mathrm{ND}} = \frac{(m^*)^2}{2\hbar^2(k_1+k_2)^2\pi R}\left[\, k_1\mathrm{e}^{2\mathrm{i}k_1R} - k_2\, \mathrm{e}^{2\mathrm{i}k_2R}\,\right]. \tag{48}$$

From the expressions above we notice that, contrary to the terms $(G_{\mathrm{D}}^2 - G_{\mathrm{ND}}^2)$ and $G_{\mathrm{D}}\, G_{\mathrm{ND}}$, G_{D} and G_{ND} behave differently in the first and second regime.

References

[1] Dzyaloshinskii I E 1957 Thermodynamic theory of weak ferromagnetism in antiferromagnetic substances *Sov. Phys. JETP* **5** 1259
[2] Moriya T 1960 Anisotropic superexchange interaction and weak ferromagnetism *Phys. Rev.* **120** 91
[3] Bode M, Heide M, von Bergmann K, Ferriani P, Heinze S, Bilhmayer G, Kubetzka A, Pietzsch O, Blügel S and Wiesendanger R 2007 Chiral magnetic order at surfaces driven by inversion asymmetry *Nature* **447** 190–3
[4] Ferriani P, von Bergmann K, Vedmedenko E Y, Heinze S, Bode M, Heide M, Bihlmayer G, Blügel S and Wiesendanger R 2008 Atomic-scale spin spiral with a unique rotational sense: Mn monolayer on W(001) *Phys. Rev. Lett.* **101** 027201
[5] Santos B, Puerta J M, Cerda J I, Stumpf R, von Bergmann K, Wiesendanger R, Bode M, McCarty K F and de la Figuera J 2008 Structure and magnetism of ultra-thin chromium layers on W(110) *New J. Phys.* **10** 013005
[6] Schweflinghaus B, Zimmermann B, Heide M, Bihlmayer G and Blügel S 2016 Role of dzyaloshinskii-moriya interaction for magnetism in transition-metal chains at pt step edges *Phys. Rev.* B **94** 024403
[7] Menzel M, Mokrousov Y, Wieser R, Bickel J E, Vedmedenko E, Blügel S, Heinze S, von Bergmann K, Kubetzka A and Wiesendanger R 2012 Information transfer by vector spin chirality in finite magnetic chains *Phys. Rev. Lett.* **108** 197204
[8] Khajetoorians A A, Steinbrecher M, Ternes M, Bouhassoune M, dos Santos Dias M, Lounis S, Wiebe J and Wiesendanger R 2016 Tailoring the chiral magnetic interaction between two individual atoms *Nat. Commun.* **7** 10620
[9] Mankovsky S, Bornemann S, Minár J, Polesya S, Ebert H, Staunton J B and Lichtenstein A I 2009 Effects of spin–orbit coupling on the spin structure of deposited transition-metal clusters *Phys. Rev.* B **80** 014422
[10] Antal A, Lazarovits B, Udvardi L, Szunyogh L, Újfalussy B and Weinberger P 2008 First-principles calculations of spin interactions and the magnetic ground states of Cr trimers on Au(111) *Phys. Rev.* B **77** 174429
[11] Mühlbauer S, Binz B, Jonietz F, Pfleiderer C, Rosch A, Neubauer A, Georgii R and Böni P 2009 Skyrmion lattice in a chiral magnet *Science* **323** 915–9
[12] Yu X Z, Onose Y, Kanazawa N, Park J H, Han J H, Matsui Y, Nagaosa N and Tokura Y 2010 Real-space observation of a two-dimensional skyrmion crystal *Nature* **465** 901–4
[13] Romming N, Hanneken C, Menzel M, Bickel J E, Wolter B, von Bergmann K, Kubetzka A and Wiesendanger R 2013 Writing and deleting single magnetic skyrmions *Science* **341** 636–9
[14] Heinze S, von Bergmann K, Menzel M, Brede J, Kubetzka A, Wiesendanger R, Bihlmayer G and Blügel S 2011 Spontaneous atomic-scale magnetic skyrmion lattice in two dimensions *Nat. Phys.* **7** 713–8
[15] Bogdanov A N and Yablonskii D A 1989 Thermodynamically stable vortices in magnetically ordered crystals. The mixed state of magnets *Sov. Phys. JETP* **68** 101–3
[16] Roessler U K, Bogdanov A N and Pfleiderer C 2006 Spontaneous skyrmion ground states in magnetic metals *Nature* **442** 797–801
[17] Baibich M N, Broto J M, Fert A, Nguyen Van Dau F, Petroff F, Etienne P, Creuzet G, Friederich A and Chazelas J 1988 Giant magnetoresistance of (001)Fe/(001)Cr magnetic superlattices *Phys. Rev. Lett.* **61** 2472–5
[18] Crum D M, Bouhassoune M, Bouaziz J, Schweflinghaus B, Blügel S and Lounis S 2015 Perpendicular reading of single confined magnetic skyrmions *Nat. Commun.* **6** 8541
[19] Hanneken C, Otte F, Kubetzka A, Dupé B, Romming N, von Bergmann K, Wiesendanger R and Heinze S 2015 Electrical detection of magnetic skyrmions by tunnelling non-collinear magnetoresistance *Nat. Nanotech.* **10** 1039–42
[20] Hamamoto K, Ezawa M and Nagaosa N 2016 Purely electrical detection of a skyrmion in constricted geometry *Appl. Phys. Lett.* **108** 112401
[21] Jonietz F *et al* 2010 Spin transfer torques in MnSi at ultralow current densities *Science* **330** 1648–51
[22] Parkin S S P, Hayashi M and Thomas L 2008 Magnetic domain-wall racetrack memory *Science* **320** 190–4
[23] Smith D A 1976 New mechanisms for magnetic anisotropy in localised s-state moment materials *J. Magn. Magn. Mater.* **1** 214–25
[24] Fert A and Levy P M 1980 Role of anisotropic exchange interactions in determining the properties of spin-glasses *Phys. Rev. Lett.* **44** 1538–41
[25] Ruderman M A and Kittel C 1954 Indirect exchange coupling of nuclear magnetic moments by conduction electrons *Phys. Rev.* **96** 99–102
[26] Kasuya T 1956 A theory of metallic ferro- and antiferromagnetism on zener's model *Prog. Theor. Phys.* **16** 45–57
[27] Yosida K 1957 *Magn. Properties Cu-Mn Alloys* **106** 893–8
[28] Zhou L, Wiebe J, Lounis S, Vedmedenko E, Meier F, Blügel S, Dederichs P H and Wiesendanger R 2010 Strength and directionality of surface Ruderman-Kittel-Kasuya-Yosida interaction mapped on the atomic scale *Nat. Phys.* **6** 187–91
[29] Khajetoorians A A, Wiebe J, Chilian B, Lounis S, Blügel S and Wiesendanger R 2012 Atom-by-atom engineering and magnetometry of tailored nanomagnets *Nat. Phys.* **8** 497–503
[30] Prüser H, Dargel P E, Bouhassoune M, Ulbrich R G, Pruschke T, Lounis S and Wenderoth M 2014 Interplay between the Kondo effect and the ruderman-kittel-kasuya-yosida interaction *Nat. Commun.* **5** 5417
[31] Imamura H, Bruno P and Utsumi Y 2004 Twisted exchange interaction between localized spins embedded in a one- or two-dimensional electron gas with rashba spin–orbit coupling *Phys. Rev.* B **69** 121303

Q2

[32] Rashba E I 1960 Svoistva poluprovodnikov s petlei ekstremumov: I. Tsiklotronnyi i kombinirovannyi rezonans v magnitnom pole, perpendikulyarnom ploskosti petli, fizika tverd. tela. *Sov. Phys. Solid State* **2** 1109
[33] Bychkov Y A and Rashba E I 1984 Svoistva dvumernogo elektronnogo gaza so snyatym vyrozhdeniem spektra *J. Phys. C: Solid State Phys.* **17** 6039
[34] Zhu J-J, Yao D-X, Zhang S-C and Chang K 2011 Electrically controllable surface magnetism on the surface of topological insulators *Phys. Rev. Lett.* **106** 097201
[35] LaShell S, McDougall B A and Jensen E 1996 Spin splitting of an Au(111) surface state band observed with angle resolved photoelectron spectroscopy *Phys. Rev. Lett.* **77** 3419–22
[36] Lounis S, Bringer A and Blügel S 2012 Magnetic adatom induced skyrmion-like spin texture in surface electron waves *Phys. Rev. Lett.* **108** 207202
[37] Walls J D and Heller E J 2007 Spin-orbit coupling induced interference in quantum corrals *Nano Lett.* **7** 3377–82
[38] Fiete G A and Heller E J 2003 *Colloquium*: theory of quantum corrals and quantum mirages *Rev. Mod. Phys.* **75** 933–48
[39] Ebert H and Mankovsky S 2009 Anisotropic exchange coupling in diluted magnetic semiconductors: *Ab initio* spin-density functional theory *Phys. Rev.* B **79** 045209
[40] Lloyd P and Smith P V 1972 Multiple scattering theory in condensed materials *Adv. Phys.* **21** 69–142
[41] Liechtenstein A I, Katsnelson M I, Antropov V P and Gubanov V A 1987 Local spin density functional approach to the theory of exchange interactions in ferromagnetic metals and alloys *J. Magn. Magn. Mater.* **67** 65–74
[42] Udvardi L, Szunyogh L, Palotás K and Weinberger P 2003 First-principles relativistic study of spin waves in thin magnetic films *Phys. Rev.* B **68** 104436
[43] Bouaziz J, Lounis S, Blügel S and Ishida H 2016 Microscopic theory of the residual surface resistivity of rashba electrons *Phys. Rev.* B **94** 045433
[44] Šipr O, Mankovsky S, Polesya S, Bornemann S, Minár J and Ebert H 2016 Illustrative view on the magnetocrystalline anisotropy of adatoms and monolayers *Phys. Rev.* B **93** 174409
[45] Kim K-W, Lee H-W, Lee K-J and Stiles M D 2013 Chirality from interfacial spin–orbit coupling effects in magnetic bilayers *Phys. Rev. Lett.* **111** 216601
[46] Lounis S 2014 Non-collinear magnetism induced by frustration in transition-metal nanostructures deposited on surfaces *J. Phys.: Condens. Matter* **26** 273201
[47] Bihlmayer G, Rader O and Winkler R 2015 Focus on the rashba effect *New J. Phys.* **17** 050202
[48] Koroteev Yu M, Bihlmayer G, Gayone J E, Chulkov E V, Blügel S, Echenique P M and Hofmann P 2004 Strong spin-orbit splitting on bi surfaces *Phys. Rev. Lett.* **93** 046403
[49] Pascual J I *et al* 2004 Role of spin in quasiparticle interference *Phys. Rev. Lett.* **93** 196802
[50] Ast C R, Henk J, Ernst A, Moreschini L, Falub M C, Pacilé D, Bruno P, Kern K and Grioni M 2007 Giant spin splitting through surface alloying *Phys. Rev. Lett.* **98** 186807
[51] Liebmann M *et al* 2016 Giant rashba-type spin splitting in ferroelectric gete(111) *Adv. Mater.* **28** 560–5
[52] Elmers H J *et al* 2016 Spin mapping of surface and bulk rashba states in ferroelectric α-gete(111) films *Phys. Rev.* B **94** 201403